



**HAL**  
open science

# Accurate measurement of curvilinear shapes by Virtual Image Correlation

Benoit Semin, Harold Auradou, Marc Louis Maurice François

► **To cite this version:**

Benoit Semin, Harold Auradou, Marc Louis Maurice François. Accurate measurement of curvilinear shapes by Virtual Image Correlation. The European Physical Journal A, 2011, 56 (1), pp.10701-1-10. 10.1051/epjap/2011110275 . hal-00442849v2

**HAL Id: hal-00442849**

**<https://hal.science/hal-00442849v2>**

Submitted on 16 Oct 2023

**HAL** is a multi-disciplinary open access archive for the deposit and dissemination of scientific research documents, whether they are published or not. The documents may come from teaching and research institutions in France or abroad, or from public or private research centers.

L'archive ouverte pluridisciplinaire **HAL**, est destinée au dépôt et à la diffusion de documents scientifiques de niveau recherche, publiés ou non, émanant des établissements d'enseignement et de recherche français ou étrangers, des laboratoires publics ou privés.

# Accurate measurement of curvilinear shapes by Virtual Image Correlation

B. Semin, H. Auradou, and M.L.M. François<sup>a</sup>

Laboratoire FAST, Université Pierre et Marie Curie Paris 6, Université Paris-Sud 11, CNRS, Bat. 502, Campus Universitaire, 91405 Orsay, France

**Abstract.** The proposed method allows the detection and the measurement, in the sense of metrology, of smooth elongated curvilinear shapes. Such measurements are required in many fields of physics, for example: mechanical engineering, biology or medicine (deflection of beams, fibers or filaments), fluid mechanics or chemistry (detection of fronts). Contrary to actual methods, the result is given in an analytical form of class  $C^\infty$  (and not a finite set of locations or pixels) thus curvatures and slopes, often of great interest in science, are given with good confidence. The proposed Virtual Image Correlation (VIC) method uses a virtual beam, an image which consists in a lateral expansion of the curve with a bell-shaped gray level. This figure is deformed until it fits the best the physical image with a method issued from the Digital Image Correlation method in use in solid mechanics. The precision of the identification is studied in a benchmark and successfully compared to two state-of-the-art methods. Three practical examples are given: a bar bending under its own weight, a thin fiber transported by a flow within a fracture and a thermal front. The first allows a comparison with theoretical solution, the second shows the ability of the method to deal with complex shapes and crossings and the third deals with ill-defined image.

## 1 Introduction

The precise and accurate determination of the shape and position of elongated objects such as hair [1], pulp fibers [2], needles [3], biological filaments [4, 5] or abiological objects [6, 7] is of interest in various scientific and technical domains. According to the beam theory [8], the curvature is of importance as it is related to the bending moment. In fluid mechanics [9–12], or chemistry, the line to be identified can be a front (temperature, concentration, etc.). In this case, the knowledge of the normal vectors, related to the angles of tangents, can be needed for a flux computation. In fracture mechanics, it may be useful to determine the equation of the decohesion front [13]. In image processing, angles and curvatures are parameters permitting to compare different shapes [14].

Such analysis can already be done with various methods. The main objective of the ridge detection methods used in the image processing field is the ability to detect curves in a noisy image. Our method is more focused on the accuracy of the detection of a unique curve. Ridge enhancing filters [15–17], as well as efficient phase congruency methods [18], emphasize pixels belonging to a ridge. Such methods require a sorting and a filtering that influence the final result. In a similar way, beamlet theories [19] results consist in a collection of segments which still

requires filtering in order to obtain the derivatives. We retained the two methods giving the best accuracy for comparison with ours. The first is Steger’s method [20] which uses the Hessian of the Gaussian filtered image [21, 22]. The second is the Fast Marching Algorithm [23], one of the Minimal Path methods [24–26].

The proposed VIC method computes the equation of the shape (thus simultaneously local angles and curvatures), with a sub-pixel precision and without filtering. The elongated object shape, from now referred to as “physical beam”, is identified by its correlation with a “virtual beam” (the word “beam” refers to the theory of Beam Mechanics [8] and denotes here a curvilinear thick line). The virtual beam mean line is defined from a truncated series expansion of its curvatures whose coefficients are iteratively varied until the virtual beam best fits the physical one. For a light physical beam over a dark background, the virtual beam has a smooth symmetric gray level distribution decreasing from white at the mean line (the middle of the virtual beam) to black at the borders. As a consequence it consists of a regular and smooth image with an analytical expression. The optimal coefficients are given by the minimization of the quadratic distance between physical and virtual beam images. This optimization step is similar to the one used by Hild and Roux [27] in their version of the Digital Image Correlation method (DIC). The DIC [28–31] allows the measurement of

<sup>a</sup> e-mail: marc.francois@univ-nantes.fr

a displacement field from two images of a solid body: one in the unstrained state and the other in the strained state. The problem we address is different as only one image is available and the body is unidimensional (the DIC requires a textured image impossible to realize in our cases where the physical beam width may be close to the pixel size).

Section 2 presents the unidimensional version of the VIC method. Key points of the method are introduced. The minimization algorithm requires an initialization detailed in Section 3. It consists of a segment by segment identification which provides a set of equidistant points lying, already with a sub-pixel precision, onto the mean line of the physical beam. The core of the method is explained in Section 4: first, the virtual beam parameterization is detailed; then the optimization method is presented, both from analytical and numerical points of view. Section 5 is devoted to the quantitative validation of the method. A reference image is built from an analytical spiral, discretized with different bit depths and levels of noise. The positions, angles and curvatures are compared to exact values. Section 6 shows three practical examples. The first one, a bar bending under its own weight, allows the validation of the method on a real experiment by comparison to the theoretical result. The second one consists of the extraction from a noisy image of a fiber flowing in a rough fracture. The last example considers the analysis of a discontinuous, scattered and very low contrasted isothermal front.

## 2 The unidimensional case

We consider a 1D image  $F$  obtained from the discretization of a continuous 1D image  $f$ . The latter has a symmetry axis (which corresponds to the mean line in the 2D case): the objective is to recover this axis from the knowledge of  $F$ .

In Figure 1a,  $f$  is depicted by a half-cosine function  $f(x) = \cos(x - x_s)$  if  $(x - x_s) \in [-\pi/2, \pi/2]$  and  $f(x) = 0$  elsewhere. This distribution qualitatively represents the gray level distribution along one cross-section of the physical beam images presented in Section 6.1 or 6.2. The corresponding digital image  $F$  is computed as the average of  $f$  over each pixel (of width 1). Due to the chosen shift  $x_s = 2.4$ , noninteger nor half-integer,  $F$  has no symmetry axis.

The estimation  $x_F$  (of the symmetry axis  $x_s$ ) is obtained from the correlation of  $F$  and the virtual image  $g$  defined as:

$$g(r) = \frac{1}{2} \left( 1 + \cos\left(\frac{\pi r}{R}\right) \right), \quad r \in [-R, R], \quad (1)$$

in which  $r = x - x_t$ ,  $2R$  is the virtual image width and  $x_t$  is the trial value. Like  $f$ , the function  $g$  has a symmetry axis but is only roughly of the same width and shape as  $f$ . It is displayed in Figure 1b for  $R = \pi$  (the width of  $g$  is then twice the width of  $f$ ) and for  $x_t = 2$ .

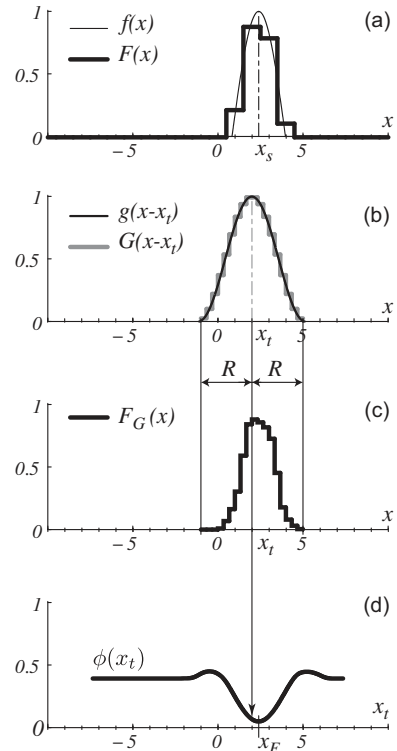


Fig. 1. Example of the method in the unidimensional case.

The correlation function  $\phi$  is the mean square deviation between  $g$  and  $f$ :

$$\phi(x_t) = \frac{1}{2R} \int_{-R}^R (f(x_t + r) - g(r))^2 dr, \quad (2)$$

and the measure consists of  $x_F = \arg \min(\phi(x_t))$ .

This expression is computed by using a thin mesh (three times finer than the pixel size in Fig. 1b) associated to  $g$ . Due to its analytical expression (Eq. (1)),  $g$  is easily digitalized into  $G$  on the fine mesh and  $F$ , defined on the pixel grid, is interpolated on the fine mesh as  $F_G$  thanks to a cubic interpolation (tested to present a good compromise between accuracy and CPU time) (Fig. 1c). The minimum of  $\phi(x_t)$  is computed here by a standard Matlab minimization procedure.

In the example (Fig. 1), one finds  $x_F = 2.394$  pixels for  $x_s = 2.4$ . The identification is clearly sub-pixel while  $F$  has only four significant pixels. Such precision is also obtained when changing the shape of  $f$  (triangle, rectangle), its contrast, luminosity or width (data not shown). Figure 1d shows that  $\phi$  is convex only in the vicinity of  $x_F$ : this justifies, in 1 or 2D, the computation of an approximate solution before the analytical determination.

## 3 Preliminary segment by segment identification of the beam shape

Before the precise identification using the continuous analytical virtual beam, the mean line is identified “segment

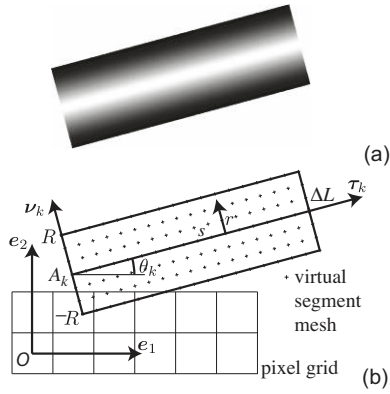


**Fig. 2.** Virtual straight segment. (a) Gray levels. (b) Parameterization and discretization.

by segment". At each step, a segment is identified by correlation between the digital image and a virtual segment (a small straight virtual beam).

The virtual image  $g$  consists here of an extrusion of the 1D virtual image used in Section 2. The coordinates ( $s \in [0, \Delta L], r \in [-R, R]$ ) of its points are referred to the local frame ( $A_k, \tau_k, \nu_k$ ) (Fig. 2). The gray level decays from the mean line to the edges:

$$g(r, s) = \frac{1}{2} \left( 1 + \cos \left( \frac{\pi r}{R} \right) \right). \quad (3)$$

The segment is positioned by  $A_k$  and the angle  $\theta_k = (\mathbf{e}_1, \tau_k)$ , where  $(O, \mathbf{e}_1, \mathbf{e}_2)$  is the reference frame of the physical image. We refer to  $g(\theta; A_k)$  as the virtual image after translation  $OA_k$  and rotation of angle  $\theta$  (Fig. 2a). The initial point  $A_k$  is set as the center of the previous segment and  $\theta_k = \arg \min(\phi)$  corresponds to the best fit (similarly to Eq. (2)) between  $f$  and  $g$ :

$$\phi(\theta) = \frac{1}{2R\Delta L} \iint_{D_g} (f - g(\theta; A_k))^2 dS, \quad (4)$$

where  $D_g$  is the definition domain of  $g$  and  $dS$  is the surface element. The initial value for the minimization is set to  $\theta_{k-1}$  so that, for examples that present beam crossing points (Fig. 14), this strategy chooses preferentially the straightest (lowest curvature) path.

As in Section 2, the virtual image  $g$  is discretized in  $G$  over a mesh, thinner than the pixel size, constituted of equally spaced points of  $R/p < 1$  along  $\tau$  and  $\Delta L/q < 1$  along  $\nu$  (see Fig. 2b). The user selects the origin point of the first segment  $A_1$ , the width  $2R$  of the virtual beam sections (slightly larger than the width of the physical beam) and the aspect ratio  $\Delta L/2R$  (generally set to 3). At each trial value of  $\theta$ ,  $\phi$  is computed using  $G$  and  $F_G$  (where  $F_G$  is the cubic interpolation of  $F$  on the fine mesh of  $G$ ). As this computation concerns only  $(2p+1)(q+1)$  points (126 in Fig. 2), the computation time remains very small. The algorithm stops at the end of the beam where the correlation is lost ( $\phi(\theta_k)$  increases suddenly). The result of this identification is a collection of equally spaced points  $A_k$  (with  $1 \leq k \leq K$ ) which approximates the mean line of the beam by a polygonal line (see, for example, Fig. 6b).

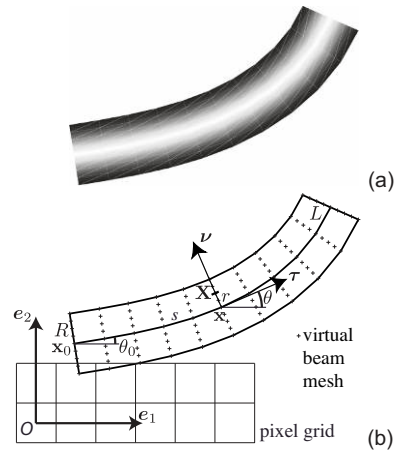


**Fig. 3.** Virtual beam. (a) Gray levels. (b) Parameterization and discretization.

## 4 Analytical shape determination

This section details the second and main step of the VIC method: the analytical identification of the mean line of the beam. The virtual segments collection considered in the previous procedure is replaced by a unique and continuous curvilinear virtual beam.

### 4.1 Parameterization of the virtual image

The curvature field  $\gamma(s)$  (where  $s$  is the curvilinear abscissa) of the mean line of the virtual beam is given by a truncated series:

$$\gamma(s) = \sum_{n=0}^N A_n P_n(\tilde{s}), \quad (5)$$

where  $\tilde{s} = s/L \in [0, 1]$  is the reduced abscissa,  $L$  is the beam length, and  $P_n$  are the  $N+1$  dimensionless basis functions. In order to guarantee the uniqueness of the coefficients, Legendre or Fourier orthogonal basis is chosen. The angle  $\theta(s)$  between the  $\mathbf{e}_1$  axis and the unit tangent vector  $\tau(s) = \cos(\theta)\mathbf{e}_1 + \sin(\theta)\mathbf{e}_2$  (see Fig. 3) is given by the integration of the previous relation:

$$\theta(s) = \theta_0 + L \sum_{n=0}^N A_n Q_n(\tilde{s}) \quad (6)$$

with

$$Q_n(\tilde{s}) = \int_0^{\tilde{s}} P_n(\tilde{\xi}) d\tilde{\xi}, \quad (7)$$

which, for Legendre or Fourier series, has an analytical expression. The integration constant  $\theta_0 = \theta(0)$  is the angle at the origin of the beam. A current point of the mean line  $\mathbf{x}$  is given by:

$$\mathbf{x} = \mathbf{x}_0 + \int_0^s \tau(\xi) d\xi, \quad (8)$$

where  $\mathbf{x}_0$  is the origin of the mean line. The virtual beam points  $\mathbf{X}$  are at the distance  $r \in [-R, R]$  to the corresponding point  $\mathbf{x}$  of the mean line:

$$\mathbf{X} = \mathbf{x} + r\boldsymbol{\nu}, \quad (9)$$

where  $\boldsymbol{\nu}$  is the normal unit vector. Points  $\mathbf{X}$  are uniquely defined since the non-overlapping condition

$$|\gamma|R < 1 \quad (10)$$

is fulfilled (else the curvature radius is smaller than  $R$  and cross-sections locally intersect). Similarly to the previous sections, the gray level of the virtual beam is:

$$g(r, s) = \frac{1}{2} \left( 1 + \cos \left( \frac{\pi r}{R} \right) \right). \quad (11)$$

Fully defined by the constants  $R, L$  and the set  $\mathbf{V} = \{\mathbf{x}_0, \theta_0, \Lambda_n\}$  of  $N + 4$  variables, the virtual image is now referred to as  $g(\mathbf{V})$ .

## 4.2 Correlation between physical and virtual beam images

The mean square deviation between virtual and physical beam images is:

$$\Phi(\mathbf{V}) = \frac{1}{2RL} \iint_{D_g} (f - g(\mathbf{V}))^2 dS, \quad (12)$$

in which  $2RL$  is the surface of the virtual beam,  $dS = (1 - \gamma r)dr ds$  the differential surface element,  $D_g$  the definition domain of  $g$ ,  $r \in [-R, R]$  and  $s \in [0, L]$ . This expression requires that  $D_g$  is fully contained in  $D_f$ , the definition domain of  $f$  (in other words the virtual image does not exceed the physical one). When  $\Phi$  is minimum, the condition  $\partial\Phi/\partial\mathbf{V} = \mathbf{0}$  is fulfilled. Naming  $V_m$  the  $m$ th term of  $\mathbf{V}$  and considering  $\partial g/\partial V_m = \mathbf{grad}(g) \cdot \partial\mathbf{X}/\partial V_m$ , one obtains:

$$\oint_{\partial D_g} (f - g)^2 \mathbf{n} \cdot \frac{\partial\mathbf{X}}{\partial V_m} dl - 2 \iint_{D_g} (f - g) \mathbf{grad}(g) \cdot \frac{\partial\mathbf{X}}{\partial V_m} dS = 0, \quad (13)$$

where  $\partial D_g$  is the external boundary of the virtual beam,  $dl$  its differential line element and  $\mathbf{n}$  its outer normal vector. We show in Appendix A that the first boundary term is negligible as soon as  $\partial D_g$  lies in the background of the beam image. Hence, the problem reduces to:

$$\iint_{D_g} (f - g) \mathbf{grad}(g) \cdot \frac{\partial\mathbf{X}}{\partial V_m} dS = 0. \quad (14)$$

This problem is solved iteratively with a Newton scheme. We call  $\Delta\mathbf{V}$  the increment of the current set of parameters  $\mathbf{V}$ . The Taylor expansion of  $g$ , up to the first order, is:

$$g(\mathbf{V} + \Delta\mathbf{V}) = g(\mathbf{V}) + \mathbf{grad}(g) \cdot \frac{\partial\mathbf{X}}{\partial V_j} \Delta V_j, \quad (15)$$

where  $j$  is a summed index. Supposing that equation (14) is fulfilled for  $g(\mathbf{V} + \Delta\mathbf{V})$  gives:

$$\begin{aligned} \Delta V_j \iint_{D_g} \left( \mathbf{grad}(g) \cdot \frac{\partial\mathbf{X}}{\partial V_m} \right) \left( \mathbf{grad}(g) \cdot \frac{\partial\mathbf{X}}{\partial V_j} \right) dS \\ = \iint_{D_g} \left( \mathbf{grad}(g) \cdot \frac{\partial\mathbf{X}}{\partial V_m} \right) (f - g) dS. \end{aligned} \quad (16)$$

This equation can be rewritten in a matrix form:

$$M_{mj} \Delta V_j = B_m, \quad (17)$$

which represents a simple linear square matrix problem whose solution  $\Delta\mathbf{V}$  is used to update the shape of the virtual beam. The term  $\mathbf{grad}(g) \cdot \partial\mathbf{X}/\partial V_m$  is involved in both the expressions of  $M_{mj}$  and  $B_m$ . From equation (11) and the beam geometry follows:

$$\mathbf{grad}(g) = \frac{\partial g}{\partial r} \boldsymbol{\nu}, \quad (18)$$

and, from equation (9):

$$\frac{\partial\mathbf{X}}{\partial V_m} = \frac{\partial\mathbf{x}}{\partial V_m} - r \frac{\partial\theta}{\partial V_m} \boldsymbol{\tau}. \quad (19)$$

The second term, orthogonal to  $\mathbf{grad}(g)$ , does not need to be calculated. The derivatives of  $\partial\mathbf{x}/\partial V_m$  are obtained using equations (8) and (6):

$$\begin{aligned} \frac{\partial\mathbf{x}}{\partial x_{0,1}} = \mathbf{e}_1, \quad \frac{\partial\mathbf{x}}{\partial x_{0,2}} = \mathbf{e}_2, \\ \frac{\partial\mathbf{x}}{\partial\theta_0} = \int_0^s \boldsymbol{\nu} d\xi, \quad \frac{\partial\mathbf{x}}{\partial\Lambda_n} = L \int_0^s Q_n \boldsymbol{\nu} d\xi, \end{aligned} \quad (20)$$

where  $(x_{0,1}, x_{0,2})$  are the components of  $\mathbf{x}_0$ . The displacement of the virtual beam between two steps is close to  $(\partial\mathbf{X}/\partial V_m)\Delta V_m$  where the fields  $\partial\mathbf{X}/\partial V_m$  can be seen as the unitary displacement fields (see Fig. 4) used in the DIC method as developed by Hild and Roux [27]. The beam ends detection is not directly included in the analytical method. As a consequence, the initial point  $\mathbf{x}_0$  is fixed along the initial beam tangent  $\boldsymbol{\tau}(0)$  in order for the virtual beam not to “slide” along the physical one during the optimization. For this reason, the optimization vector is reduced to  $\mathbf{V} = \{x_{0,\nu}, \theta_0, \Lambda_n\}$ , where  $x_{0,\nu}$  denotes the remaining normal free component of  $\mathbf{x}_0$ .

## 4.3 Numerical aspects

The virtual beam  $g$  is discretized (and then referred to, as in Sects. 2 and 3, as  $G$ ) over a fine mesh obtained from the discretization of the curvilinear frame  $(s, r)$ , each  $\Delta L = L/q$  along  $s$  and  $\Delta R = R/p$  along  $r$  (see Fig. 3). Again, this mesh of  $(2p + 1)(q + 1)$  points is chosen finer than the pixel size. The digital image  $F$  is projected (with a bi-dimensional cubic interpolation) onto it, giving  $F_G$  which is used for the computation of equation (16). The iterative process is repeated until the value of  $\Phi$  decreases by

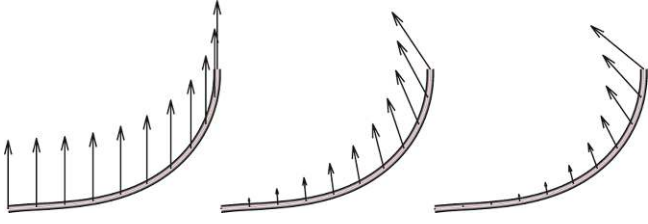


**Fig. 4.** (Color online) Examples of unitary displacement fields. From left to right:  $\partial \mathbf{x} / \partial x_{0,2}$  (vertical translation),  $\partial \mathbf{x} / \partial \theta_0$  (rotation) and  $\partial \mathbf{x} / \partial \lambda_0$  (uniform increase of the curvature).

less than a prescribed amount ( $10^{-6}$ ) between two steps. It converges generally in less than 10 iterations.

Initial parameters  $\mathbf{V}^0 = \{\mathbf{x}_0^0, \theta_0^0, \Lambda_n^0\}$  are computed from the data  $\{A_k, \theta_k\}$  given by the segment by segment identification (Sect. 3). The length of the beam  $L = K \Delta L$  is kept. For the other terms, we consider the following equation, which consists of an extension of equation (6), supplemented by  $\Lambda_{-1} = \theta_0/L$  and  $Q_{-1}(\tilde{s}) = 1$ :

$$\frac{\theta(s)}{L} = \sum_{n=-1}^N \Lambda_n Q_n(\tilde{s}). \quad (21)$$

Ideally, it applies for each couple  $(\theta_k, s_k)$ , where  $s_k = k \Delta L$ , given by the segment by segment analysis. In general,  $N \ll K$  and the matrix system that corresponds to this equation is overdefined. Consequently, initial parameters  $\Lambda_n^0$  are given by the numerical minimization of the least square deviation  $\Xi(\Lambda_n)$ :

$$\Xi(\Lambda_n) = \sum_{k=1}^K \left( \sum_{n=-1}^N \Lambda_n^0 Q_n \left( \frac{s_k}{L} \right) - \frac{\theta_k}{L} \right)^2. \quad (22)$$

## 5 Performance evaluation

In this section, the precision and the robustness of the method is tested with respect to bit depth and noise level. An image of a beam is generated from an analytical spiral, a curve involving large curvature variations. The method is applied to digitalized images of this beam, with various bit depths and added noise. Positions, angles, curvatures and series coefficients given by the method are compared to the exact ones.

### 5.1 The reference synthetic image

The mean line of the synthetic beam consists of a logarithmic spiral whose equation is  $\rho^* = ab^\psi$  in polar coordinates  $(\rho^*, \psi)$ . The values used for Figure 5 are  $a = 8$ ,  $\ln(b) = 1/\tan(11\pi/24)$  and  $0 \leq \psi \leq 7\pi$ . The choice of this shape is motivated by the existence of an analytical expression of radius, angle and curvature and the wide range of curvature variation ( $1/146 \lesssim \gamma^* \lesssim 1/8 \text{ pixel}^{-1}$  here).

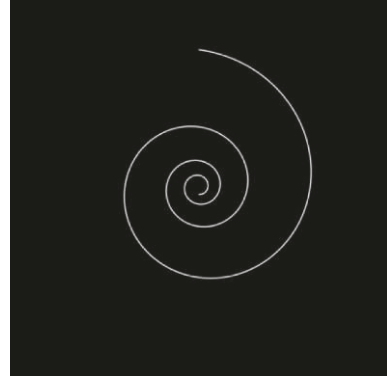


**Fig. 5.** Synthetic  $401 \times 401$  pixels 8-bit noiseless image.

The analytical expression of the spiral curvature  $\gamma^*$  allows the computation of the exact values of the series parameters  $\Lambda_n^*$  given by (using Eq. (5) and the orthogonality of the basis):

$$\Lambda_n^* \int_0^1 P_n^2(\tilde{s}) d\tilde{s} = \int_0^1 \gamma^*(\tilde{s}) P_n(\tilde{s}) d\tilde{s}. \quad (23)$$

The synthetic beam image, built from this mean line, has a thickness  $2R^* = 2$  pixels. Its luminance is assumed to follow a half-cosine distribution  $l^*(r, s) = \cos(\pi r/2R^*)$  for  $r \in [-R^*, R^*]$ . As in the unidimensional example (Sect. 2) this distribution differs from that of the virtual beam. This image is discretized in space in a  $401 \times 401$  pixels digital image  $F$ . The resulting image is discretized in 1, 8 (see Fig. 5) or 16 bits. A close-up of the 8-bit image is shown in Figure 6a at the pixel scale.

The evaluation of the methods consists in comparing exact (starred) and measured values of the radius, angles (from the horizontal axis to the tangent) and curvatures, respectively by  $\Delta\rho = \rho^* - \rho$ ,  $\Delta\theta = \theta^* - \theta$  and  $\Delta\gamma = \gamma^* - \gamma$ , with respect to their evolution along the polar angle  $\Psi$ . Moreover, a visual information is given by Figures 6, 8 and 9 in which the exact spiral is the thick black line (of 1 pixel width) and the measured shape is the thin light one.

### 5.2 Tests on 8-bit noiseless image

At first, the segment by segment identification is applied to the image. The parameter  $R$  is set to 1 pixel and the mesh of the virtual segment is chosen three times finer than the pixel size. Figure 6b shows that the segments are already well positioned with respect to the exact spiral location. Figure 7a shows that the precision is sub-pixel. More precisely, the mean square distance between exact and measured points is  $\sigma(\Delta\rho) = 0.100$  pixel. The discrepancy increases in high-curvature regions where straight segments are less adapted.

At second, the analytical identification is proceeded. Legendre series with orders  $N = [6, 7, 8, 9, 10, 12, 15, 20]$  are used. The virtual beam mesh is three times finer than

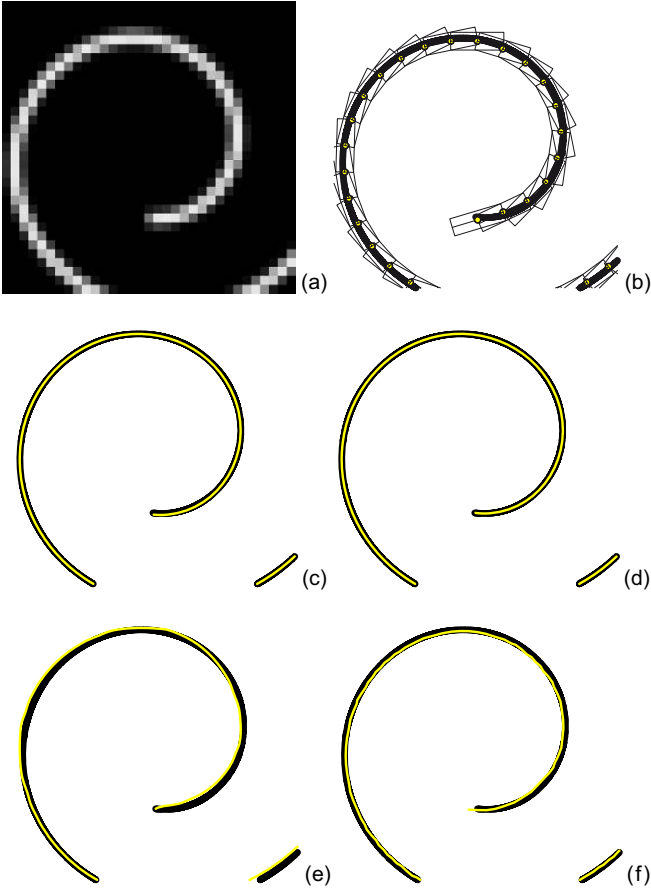


**Fig. 6.** (Color online) Noiseless 8-bit spiral image close-up. (a) Original image. (b) Segment by segment detection. (c) VIC method,  $N = 12$ . (d) VIC method,  $N = 20$ . (e) Fast Marching Algorithm. (f) Steger's method.

the pixel grid. The identified curve begins to match the whole spiral at  $N = 7$ . At  $N = 12$  the theoretical spiral shape is almost perfectly recovered (Fig. 6c) and  $\sigma(\Delta\rho) = 0.029$  pixel. At  $N = 20$  the two curves are undistinguishable (Fig. 6d) and  $\sigma(\Delta\rho) = 0.009$  pixel. Figure 7a shows that the precision of the identification continuously increases with the order  $N$  of the series. However, orders too high must be avoided because they allow high frequency tortuosity thus the identification may be influenced by the pixel grid. Various trials have shown the weak influence of the user-defined radius  $R$  of the virtual beam. Figures 7b and 7c illustrate the ability of the method to measure angles and curvatures with confidence. The exact series coefficients  $\Lambda_n^*$  are also successfully compared to the  $\Lambda_n$  obtained by the analytical identification, at order  $N = 20$  in Figure 7d. Moreover, it has been verified that each  $\Lambda_n$  varies smoothly and reversibly when the order  $N$  of the series is changed.

The VIC method is compared to the retained reference ones (see Sect. 1). The Fast Marching Algorithm (FMA) [32] (the Matlab toolbox of [33] is used) gives at best a precision  $\sigma(\Delta\rho) = 0.370$  pixel (Fig. 6e) when setting the mean square deviation of the Gaussian filter at  $\sigma_G = 0.5$  pixel. Steger's method gives at best a precision

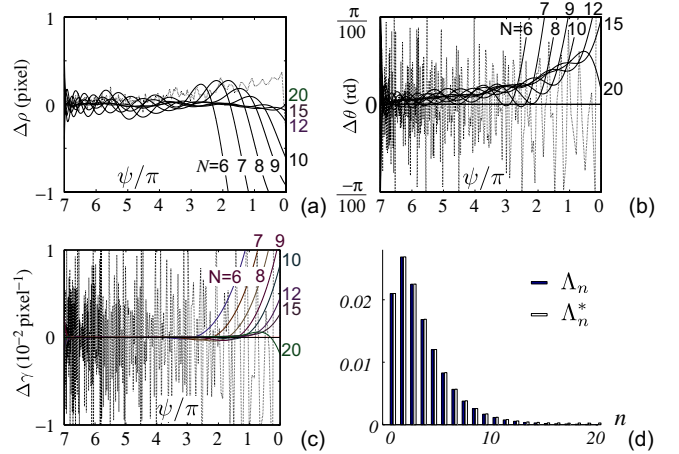


**Fig. 7.** (Color online) Identification error. (a) Distance, (b) angle and (c) curvature. Thin dotted line: segment by segment identification, thick lines: analytical identification. (d) Series coefficients comparison.

of  $\sigma(\Delta\rho) = 0.083$  pixel (Fig. 6f) when setting  $\sigma_G = 2$  pixels, better than the FMA but approximately 10 times worse than the VIC.

### 5.3 Noise and bit depth influences

An uncorrelated Gaussian noise image  $G_N$ , with a standard deviation  $\sigma_N = 1$ , is generated. Working images are defined as  $F + \sigma_N G_N$  with  $0 \leq \sigma_N \leq 1$ , off limits data are truncated and the image is digitalized in 8 bits.

For  $\sigma_N = 30\%$  (Fig. 8a) the segment by segment identification succeeds to follow the spiral from the outer to the center point and, despite the added noise, the mean square distance between measured and identified radii is still sub-pixel with  $\sigma(\Delta\rho) = 0.128$  pixels (Fig. 8b). From this preliminary identification the analytical method is proceeded successively with  $N = 12$  and  $N = 20$  (Fig. 8c and d) and gives  $\sigma(\Delta\rho) = 0.054$  in that last case. These results can successfully be compared to the one obtained with the chosen reference methods. At the best we obtain  $\sigma(\Delta\rho) = 0.477$  pixel with the Fast Marching Algorithm (setting  $\sigma_G = 1$  pixel and a threshold at 75%) and  $\sigma(\Delta\rho) = 0.212$  pixel with Steger's method (setting  $\sigma_G = 2$  pixels).

For  $\sigma_N = 50\%$  (Fig. 9a) (still an 8-bit image), the segment by segment method requires a preliminary Gaussian filter with  $\sigma_G = 2$  in order to succeed to follow the spiral and gives  $\sigma(\Delta\rho) = 0.173$  pixel. The analytical method is performed after (using the unfiltered image) and still gives a good precision:  $\sigma(\Delta\rho) = 0.085$  pixel for  $N = 20$  (Fig. 9d). From this level of noise, we did not succeed in performing the FMA and Steger's methods.

Figure 10 summarizes the results obtained up to  $\sigma_N = 50\%$  and 8-bit depth. The VIC method demonstrates its precision compared to other tested methods and its robustness with respect to noise.

At very high noise levels  $\sigma_N \geq 60\%$  the segment by segment method does not succeed even after a Gaussian

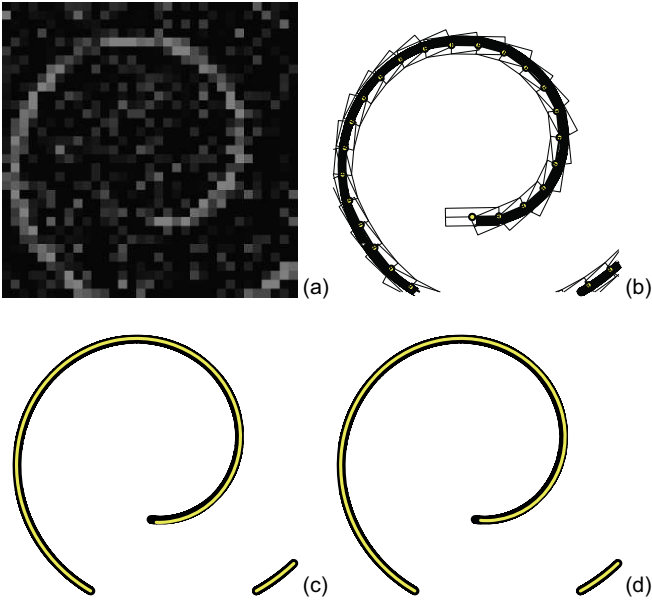


**Fig. 8.** (Color online) Thirty percent noise 8-bit spiral image close-up. (a) Original image. (b) Segment by segment detection. (c) VIC method,  $N = 12$ . (d) VIC method,  $N = 20$ .

filtering. Indeed, as one can think that methods dedicated to the ridge identification [18, 34, 35] may succeed in following the spiral, we perform in these cases the analytical method by using the segment by segment identification of Section 5.2. Figure 11 shows that, in almost every case the position is identified with a sub-pixel precision. It includes also the results for 1-bit images: the bit depth increases as expected based on the precision of the method. Other alterations have been tested (not presented): a contrast reduction, associated or not with a luminosity variation (which brightens the background), has the same effect as the bit depth variation which it induces.

## 6 Examples of application

### 6.1 A cantilever beam

The objective of this test is to show the precision of the method in a real experiment. A cantilever bar bending under its own weight has a theoretical solution [8] which will be compared to the shape obtained by the VIC. The  $2R = 5$  mm thick and  $L = 2.5$  m long bar is clamped in the chuck of a milling machine in front of a black curtain and bends under its own weight. The  $4288 \times 2848$  pixels image (Fig. 12) has been taken with a Nikon D300 camera. The VIC method is proceeded with a Legendre series of order  $N = 3$ . The identified mean line differs by less than 2 pixels (1.2 mm) from the theoretical curve computed with standard physical properties of aluminum (Young's modulus  $E = 72$  GPa and mass density  $\rho = 2700$  kg/m<sup>3</sup>). Even if the quality of the identification decreases when the derivative order increases, the angles and curvature remain of good quality (see Fig. 13).

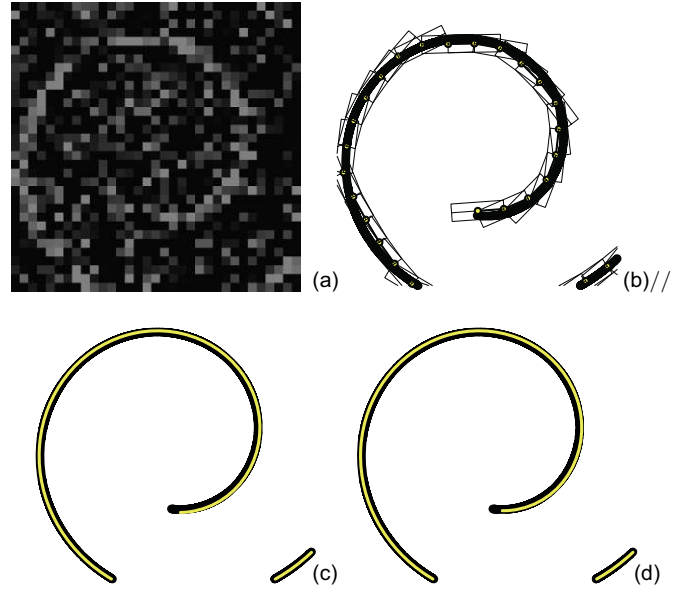


**Fig. 9.** (Color online) Fifty percent noise 8-bit spiral image close-up. (a) Original image. (b) Segment by segment detection. (c) VIC method,  $N = 12$ . (d) VIC method,  $N = 20$ .

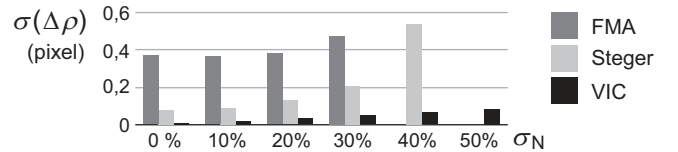


**Fig. 10.** Error for different noise level and methods (Fast Marching Algorithm, Steger's method and proposed VIC).

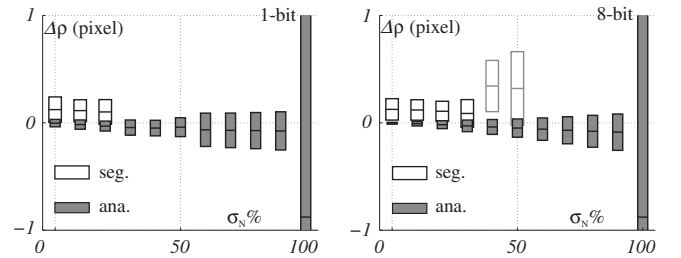


**Fig. 11.** Precision of the identification, for 1- and 8-bit depth and 11 noise levels. Mean: middle of the segments. Bar length: twice the standard deviation.

### 6.2 Fiber transported by a fluid flow in a fracture

This experiment [36] considers the motion and deformation of fibers (diameter 0.28 mm) transported by a fluid within a transparent fracture of mean aperture 0.65 mm. Figure 14 shows an example of observation; the information that are sought are, for this example, the fiber position, local angle and curvature. The latter has a major importance as, according to the beam theory [8], it is proportional to the bending moment generated here by the action of the hydrodynamic forces. The low quality and definition of the image are due to the experimental





**Fig. 12.** (Color online) Aluminium bar bending under its own weight.

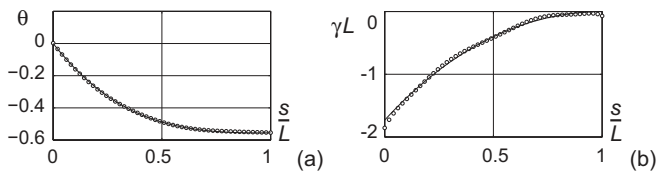


**Fig. 13.** Comparison between the beam theory (solid line) and the VIC method (circles). (a) Angles (rad). (b) Curvatures.

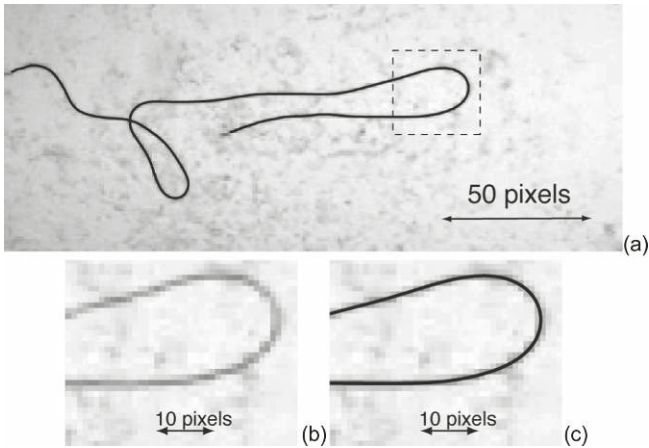


**Fig. 14.** Fiber transported by a fluid flow in a fracture. (a) Physical image and identified mean line (dotted line), for  $N = 50$ . (b) Detail view. (c) Detail view and identification.

conditions: the high speed of the fiber imposes a short exposure time and the roughness of the fracture walls induces low contrast and lots of artifacts. The apparent fiber diameter is close to 1 pixel.

The full VIC (segment by segment followed by analytical measurements) method is applied to this picture, with  $R = 1$  pixel and using Legendre series. Figure 14 shows that, despite the small radius of the object and the high noise level, the central line collapses onto the fiber along the full length. Wide meanders as well as small deviations from the straight line are perfectly followed and even the crossing does not perturb the identification.

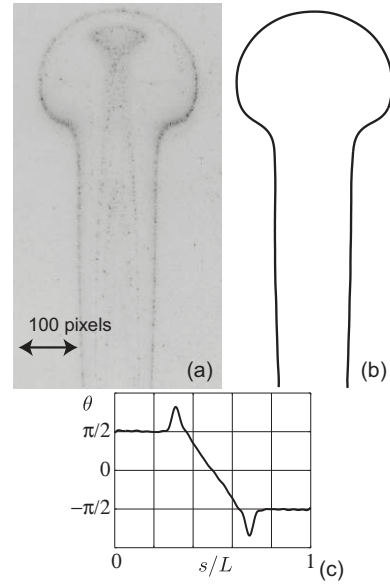


**Fig. 15.** (a) Image of the thermal plume (left, courtesy of A. Davaille and J. Vatteville). The exterior curve corresponds to the temperature  $23.6 \pm 0.2^\circ\text{C}$ . (b) Identification with the VIC method (right). (c) Angles (rad).

### 6.3 Thermal plume

Figure 15a shows an image (inverted and with enhanced contrast) of a laminar thermal plume. This experimental study was designed to better understand convection in the Earth's mantle [10,37]. The experiment consists of a tank filled with sugar syrup and containing a heating cylinder device at its bottom. The thermal plume is materialized with thermochromic liquid crystal (TLC) slurries added to the fluid illuminated by a green laser sheet. Three kinds of crystals have been used here, each one reflecting light at a different temperature. Highly scattered dark curves correspond to three different isotherms. The computation of thermal fluxes from this image requires both the accurate position and normal vectors (related to angles) of such isothermal curves.

This image is analyzed with the VIC method, using a Fourier series for  $R = 3$  and  $N = 40$ . The identification is successful (Fig. 15b) despite the noise and the discontinuity of the physical line. The angles distribution (Fig. 15c) is smooth as expected in such physical phenomenon.

## 7 Conclusion

The Virtual Image Correlation method allows one to identify precisely the shape (mean line) of a smooth curve embedded in an image, with a sub-pixel precision.

Other generic shape descriptions such as powerful Bézier curves or splines (used in Computer-Aided Design) will be soon added to the method. If available, the shape descriptor may also be an analytical solution of the physical problem [38], allowing the direct evaluation of the physical parameters which act as shape parameters (for

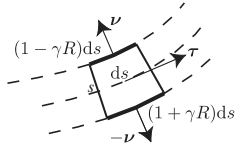


**Fig. 16.** Virtual beam boundary differential element.

example in Sect. 6.1 one may use the semi-analytical resolution and identify the parameter  $E/\rho$ .

The method can be extended to 3D and time sequences. In the latter case, the smoothness hypothesis would be extended to time, allowing the loop formation tracking. With a slight modification of the virtual beam luminance definition (step shaped), the method can also be used for edge detection problems.

Authors gratefully thank J.P. Hulin and A. Anning for their help.

## A Boundary term

We show that the first term of equation (13) vanishes under some reasonable conditions. A necessary hypothesis is that the border  $\partial D_g$  of the virtual image lies in the background of the physical image  $f$  (this assumption justifies the preliminary segment by segment identification). At first, a straightforward proof is given if one assumes that the background is uniform:  $f = f_u$ . As  $g(\mathbf{X}) = 0$  for  $\mathbf{X} \in \partial D_g$ , the divergence theorem gives:

$$\oint_{\partial D_g} (f - g)^2 \mathbf{n} \cdot \frac{\partial \mathbf{X}}{\partial V_m} dl = f_u^2 \frac{\partial}{\partial V_m} \left( \iint_{D_g} \text{div}(\mathbf{X}) dS \right) \quad (24)$$

and, as  $\text{div}(\mathbf{X}) = 2$ , the surface integral equals  $4RL$ , and its derivative with respect to  $V_m$  equals zero. Then, a weaker hypothesis can give the same result. To a differential element of the upper boundary  $\partial D_g^+$  corresponds another one on the lower part  $\partial D_g^-$ . From geometrical considerations (shown in Fig. 16) and from equation (19) comes (neglecting the small boundary parts at  $s = 0$  and  $s = L$ ):

$$\begin{aligned} \oint_{\partial D_g} (f - g)^2 \mathbf{n} \cdot \frac{\partial \mathbf{X}}{\partial V_m} dl &= \int_0^L (f^2(s, R)(1 - \gamma R) \\ &\quad - f^2(s, -R)(1 + \gamma R)) \nu \\ &\quad \cdot \frac{\partial \mathbf{x}}{\partial V_m} ds. \end{aligned} \quad (25)$$

This method is relevant for thin beams and low curvatures: we suppose  $|\gamma|R \ll 1$ . We denote by  $\lambda_c$  the correlation length of the noise, and  $\lambda_m$  a characteristic length of  $\partial \mathbf{x} / \partial V_m$ . In case of correlated noise, if  $\lambda_c \gg R$  then  $f(s, R) \simeq f(s, -R)$ . In case of uncorrelated noise, if  $1 = \lambda_c \ll \lambda_m$ ,  $f^2$  appears as a high frequency noise and the term  $f^2(s, R) - f^2(s, -R)$  vanishes statistically on a length  $\Delta L$  such as  $\lambda_c \ll \Delta L \ll \lambda_m$ . In both cases this integral is close to 0.

## References

1. C.R. Robbins, *Chemical and Physical Behavior of Human Hair*, 4th edn. (Springer Verlag, Berlin, 2002)
2. O.L. Forgacs, S.G. Mason, *J. Coll. Sci. Imp. U. Tok.* **14**, 473 (1959)
3. S.H. Okazawa, R. Ebrahimi, J. Chuang, R.N. Rohling, S.E. Salcudean, *Med. Image Anal.* **10**, 330 (2006)
4. J. Shin, L. Mahadevan, P. So, P. Matsudaira, *J. Mol. Biol.* **337**, 255 (2004)
5. W.R. DiLuzio, L. Turner, M. Mayer, P. Garstecki, D.B. Weibel, H.C. Berg, G.M. Whitesides, *Nature* **435**, 1271 (2005)
6. R. Dreyfus, J. Baudry, M. Roper, M. Fermigier, H.A. Stone, J. Bibette, *Nature* **437**, 862 (2005)
7. P. Garstecki, P. Tierno, D.B. Weibel, F. Sagués, G.M. Whitesides, *J. Phys. Condens. Matter* **21**, 204110 (2009)
8. L.D. Landau, E.M. Lifschitz, *Theory of Elasticity* (Elsevier, Amsterdam, 2006)
9. M.V. D'Angelo, H. Auradou, C. Allain, M. Rosen, J.P. Hulin, *Phys. Fluids* **20**, 1 (2008)
10. A. Davaille, A. Limare, F. Touitou, I. Kumagai, J. Vatteville, *Exp. Fluids* **50**, 285 (2010)
11. I. Bou Malham, N. Jarrige, J. Martin, N. Rakotomalala, L. Talon, D. Salin, *J. Chem. Phys.* **133**, 244505 (2010)
12. R. Planet, S. Santucci, J. Ortín, J. Contam. Hydrol. **120–121**, 157 (2011)
13. D. Dalmas, E. Barthel, D. Vandembroucq, *J. Mech. Phys. Solids* **57**, 446 (2009)
14. E.M. Arkin, L.P. Chew, D.P. Huttenlocher, K. Kedem, J.S.B. Mitchell, in *Proc. of the ACM-SIAM Symposium on Discrete Algorithms* (Society for Industrial and Applied Mathematics, Philadelphia, 1990), pp. 129–137
15. R. Haralick, *Lect. Notes Comput. Sci.* **22**, 28 (1983)
16. P.A. Toft, in *Proc. of the IEEE ICASSP-96 Conference* (IEEE Computer Society, Washington, 1996), pp. 2219–2222
17. Q. Zhang, I. Couloigner, *IEEE Trans. Image Process.* **16**, 310 (2007)
18. P. Kovsi, *J. Comput. Vis. Res.* **1**, 2 (1999)
19. D. Donoho, X. Huo, *Lecture Notes in Computational Science and Engineering* (Springer Verlag, Berlin, 2002), pp. 149–196
20. C. Steger, *IEEE Trans. Pattern Anal. Mach. Intell.* **20**, 113 (1998)
21. D. Eberly, R. Gardner, B. Morse, S. Pizer, C. Scharlach, *J. Math. Imaging Vision* **4**, 353 (1994)
22. S.R. Aylward, E. Bulitt, *IEEE Trans. Med. Imaging* **21**, 61 (2002)
23. J.A. Sethian, *Level Set Methods: Evolving Interfaces in Geometry, Fluid Mechanics, Computer Vision and Material Sciences* (Cambridge University Press, Cambridge, 1999)
24. V. Caselles, R. Kimmel, G. Sapiro, *Int. J. Comput. Vision* **22**, 61 (1997)
25. T. Deschamps, L.D. Cohen, *Med. Image Anal.* **5**, 281 (2001)
26. D. Mueller, A. Maeder, *Comput. Med. Imaging Graph* **32**, 463 (2008)
27. F. Hild, S. Roux, *Strain* **42**, 8 (2006)
28. T.C. Chu, W.F. Ranson, M.A. Sutton, W.H. Peters, *Exp. Mech.* **25**, 232 (1989)

29. F. Hild, S. Roux, C.R. Acad. Sci., Ser. IIB-Mec. **334**, 8 (2006)
30. J. Rethore, S. Roux, F. Hild, C.R. Acad. Sci., Ser. IIB-Mec. **335**, 131 (2007)
31. Y.N. Chen, W. Jin, L. Zhao, F. Li, Optik **120**, 835 (2009)
32. J.A. Sethian, *Level Set Methods and Fast Marching Methods* (Cambridge University Press, Cambridge, 1998)
33. G. Peyré, L.D. Cohen, Int. J. Comput. Vision **69**, 145 (2006)
34. T. Lindeberg, *Scale-Space Theory in Computer Vision* (Kluwer Academic, Dordrecht, 1994)
35. J.L. Starck, E.J. Candès, D.L. Donoho, IEEE Trans. Image Process. **11**, 670 (2002)
36. M.V. D'Angelo, B. Semin, G. Picard, M. Poitzsch, J.P. Hulin, H. Auradou, Transp. Porous Media **84**, 389 (2010)
37. A. Davaille, S. Androvandi, J. Vatteville, A. Limare, V. Vidal, M. Lebars, Thermal boudaries layer instabilities in viscous fluids, in *Proc. ISFV13, Nice, France, 2008*
38. M. Grédiac, E. Toussaint, F. Pierron, Int. J. Solids Struct. **39**, 2691 (2002)